Numerical Simulations of a Hall Thruster Hollow Cathode Plasma

IEPC-2007-018

Presented at the 30th International Electric Propulsion Conference, Florence, Italy
September 17-20, 2007

Ioannis G. Mikellides,* Ira Katz,† Kristina K. Jameson,‡ and Dan M. Goebel§
Jet Propulsion Laboratory, California Institute of Technology, Pasadena, CA, 91109

Abstract: The hollow cathode life models developed at JPL in the last few years have provided unique insight into the physics of the partially-ionized gas, and into the erosion mechanisms that degrade the life of these devices when used in ion propulsion. Many Hall thrusters under consideration for NASA's science missions use the same cathode technology and may therefore be subject to similar life limiting mechanisms. In general, at a given power level and discharge current, Hall thruster cathodes operate with higher gas flow rates than their ion propulsion counterparts. In this paper we present numerical simulations of a 0.635-cm (NSTAR-like) cathode for various flow rates and compare the results with measured plasma densities. The simulations include the case of 11.1 sccm and 10 A of discharge current emulating operation of a 4.5-kW Hall thruster. In agreement with the conclusions from past simulations of a larger (1.5-cm) discharge cathode on the importance of neutral gas viscosity, it is found that viscous effects remain a dominant aspect of the neutral gas flow inside the smaller cathodes where it is determined that the Reynolds number is in the order of unity. A comparison of the 2-D inviscid and viscous neutral gas flow fields shows the significant effect of viscosity on the flow field and on the balance between the pressure-gradient and ion-drag forces on the atomic species.

I. Introduction

Since its inception over three decades ago the Hall thruster's unique combination of high specific impulse and thrust-to-power ratio established it as a favored propulsion system for a variety of near-Earth space missions. In the former Soviet Union and more recently in Russia, over seventy Stationary Plasma Thrusters (SPT) have been employed onboard spacecraft since the early seventies, mainly for station keeping.[1] The 1998 launch of a Thruster with Anode Layer (TAL) on the National Reconnaissance Office's Space Technology Experiment Satellite also marked the first flight of a Hall thruster on a U.S. spacecraft.[2] Since then the technology has been flown for commercial purposes onboard the Space Systems/Loral's communications satellites MBSat, Intelstar Americas-8, and iPSTAR. Lockheed Martin Space Systems also plans to fly Aerojet's Busek-Primex Thrusters (BPT-4000) on the US Air Force Advanced-EHF defense communications satellite. Today, commercial Hall thrusters are available by Loral, Aerojet and Busek, which offers an opportunity for significant cost reductions on many science missions considered by NASA. By buying "off the assembly line" of existing product lines the cost associated with the infrequent development of thruster components for science missions may be significantly reduced.[3]

* Member Technical Staff, Electric Propulsion Group, 4800 Oak Grove Drive, Pasadena, CA, 91109, Mail Stop 125-109, Senior Member AIAA.
† Group Supervisor, Electric Propulsion Group, 4800 Oak Grove Drive, Pasadena, CA, 91109, Mail Stop 125-109, Senior Member AIAA.
‡ Academic Part Time Staff, Thermal and Propulsion Engineering Section, 4800 Oak Grove Drive, Pasadena, CA, 91109, Mail Stop 125-109, Member AIAA.
§ Section Staff, Thermal and Propulsion Engineering Section, 4800 Oak Grove Drive, Pasadena, CA, 91109, Mail Stop 125-109, Senior Member AIAA.

In general however, science missions considered by NASA have more demanding life requirements on the electric propulsion (EP) system compared to commercial missions. Thus, the employment of commercial EP onboard NASA missions based on laboratory testing alone would normally require longer and more costly thruster qualification programs. For many science missions cost caps and launch timelines would prohibit such programs. One approach that may significantly reduce cost and risk associated with long-duration life tests is to combine short-time testing with modeling. For this reason we have established at JPL a strong life modeling program consisting of rigorous, physics-based computational models as demanded by the complexity of the plasma processes associated with the degradation of thruster components. One such model is the two-dimensional (2-D) Orificed Cathode code, OrCa-2D, which solves numerically an extensive system of conservation laws for the partially-ionized gas in thermionic hollow cathodes. During the early stages of its development, OrCa2D was intended to assess processes inside the emitter region of hollow cathodes and thus excluded several physics but depended heavily on experimental measurements to account for their absence. For example, a momentum equation for the neutral gas was not included so the total pressure was assumed uniform, and was prescribed by experiment. This proved sufficient to capture the main features of the plasma for the bulk of the emitter region but was clearly insufficient to resolve accurately the details of the flow in regions close to the orifice. Since then OrCa2D has undergone considerable development and now accounts for all known physics in all regions of interest: the emitter, orifice, near-plume and (far-plume) anode. Moreover, OrCa2D no longer depends on measurements of the partially-ionized gas and thus can simulate any (conventional) thermionic hollow cathode of a given geometry, operating condition and emitter temperature. The code has recently been applied to explain the erosion patterns observed in neutralizer and discharge hollow cathodes after the completion of two long-duration life tests performed by NASA between 1997 and 2004[4,5]of the NASA Solar Electric Propulsion Technology Applications Readiness (NSTAR), 30-cm ion thruster.

Most Hall thrusters under consideration for NASA's science missions use the same cathode technology that is used in conventional ring-cusp ion propulsion, and may therefore be subject to similar life limiting mechanisms after long periods of operation. In this paper OrCa2D is employed to simulate the partially-ionized gas inside a hollow cathode for a typical Hall thruster operating condition. Though similar in geometry, Hall thruster cathodes usually operate at higher flow rates compared to discharge cathodes in ring-cusp ion thrusters. In fact, the flow rate can be several times that of ion thruster cathodes for a given discharge current. Although the peak neutral gas and the plasma concentrations are both expected to increase with increasing flow rate, implying the possibility of increased heating of the emitter by ion and/or electron bombardment, measurements of the emitter temperature in a typical NSTAR-like discharge hollow cathode have shown only a small sensitivity of the temperature on the flow rate.[6] The range examined by these measurements was 5.5-10 sccm at 12 A which includes (at the higher flow rates) typical Hall thruster cathode operation. This paper reports on preliminary findings associated with the observed plasma trends inside the cathode as the gas flow rate is increased. Specifically, the NSTAR 0.635-cm is simulated with OrCa2D for a range of flow rates. One simulation at 11.1 sccm and 10 A is included for the NSTAR cathode that emulates one operating point of the 4.5-kW Busek-Primex Thruster (BPT-4000).[7] The results at the lower flow rates (3, 4 and 5 sccm) are compared with measurements of the plasma density obtained inside these cathodes.

II. General Description of the 2-D Hollow Cathode Code OrCa2D

A. General description of the model physics

The two-dimensional numerical model solves the fluid conservation laws for three species present in the partially-ionized gas: electrons, xenon ions and xenon neutrals. It is assumed that only singly-charged ions are present and that the ionized species satisfy quasi-neutrality $n \equiv n_e = n_i$. The most general computational region is illustrated in Fig. 1. It spans the cathode interior, cathode and keeper orifices, and the cathode's near-plume and far-plume/anode regions. The gap between the keeper and cathode plates is not modeled; the imposed boundary conditions assume that the plate wall covers the gap. The computational grid consists mostly of rectangular cells inside the cathode but transitions to a generalized grid arrangement in the plume region in close alignment with the applied magnetic field, especially in regions of high field strength. In the simulations presented herein a smaller computational region has been employed for the plume, and the applied magnetic field has been excluded. These exclusions have a minimal effect on the evolution of the plasma inside the emitter region, which is the focus of this paper.

1. Conservation laws

The conservation laws for the partially-ionized gas and related boundary conditions have been presented in detail in previous articles[8,9] and will only be described briefly here. In the 2-D model, the equations of continuity and momentum for ions, and the momentum equation for the electrons are solved directly to yield the plasma particle density, ion and electron current densities. The combination of the electron and ion continuity equations yields the current conservation law which is solved for the plasma potential. The electron temperature is obtained from the electron energy transport equation. The energy equation includes thermal diffusion, energy losses due to ionization and the work done on the electrons by the electric field. The ions and neutrals are assumed to be in thermal equilibrium inside the cathode and a single equation is employed for the conservation of energy of the heavy species. Sheath boundary conditions are applied at the cathode wall boundaries that include thermionic emission from the emitter based on a prescribed temperature profile. The neutral gas density is determined by the neutral gas continuity equation which includes the ionization source term. The latter is determined based on measured ionization collision cross-sections. Inside the cathode the neutral gas satisfies the continuum assumption so the fluid momentum equation is solved to yield the neutral gas flux. For many EP the mean free paths (mfp) for neutral collisions are comparable to the characteristic dimensions somewhere inside the orifice and can be many times the keeper diameter in the keeper orifice region. In these "collisionless" regions it is assumed that the gas particles expand freely in straight-line trajectories from a pre-determined boundary, the "transition line." Because the approach relies heavily on the determination of all view factors associated with the cathode geometry, it is referred to as the "VF" (view factor) method. The collisionless region is "fed" with the solution of the fluid momentum equation inside the cathode. The two regions comprising fluid and collisionless neutrals are coupled at the transition line. The conservation equations are discretized using finite volumes, and are solved using a strongly-implicit method. The neutral gas continuity and momentum equations are solved explicitly.

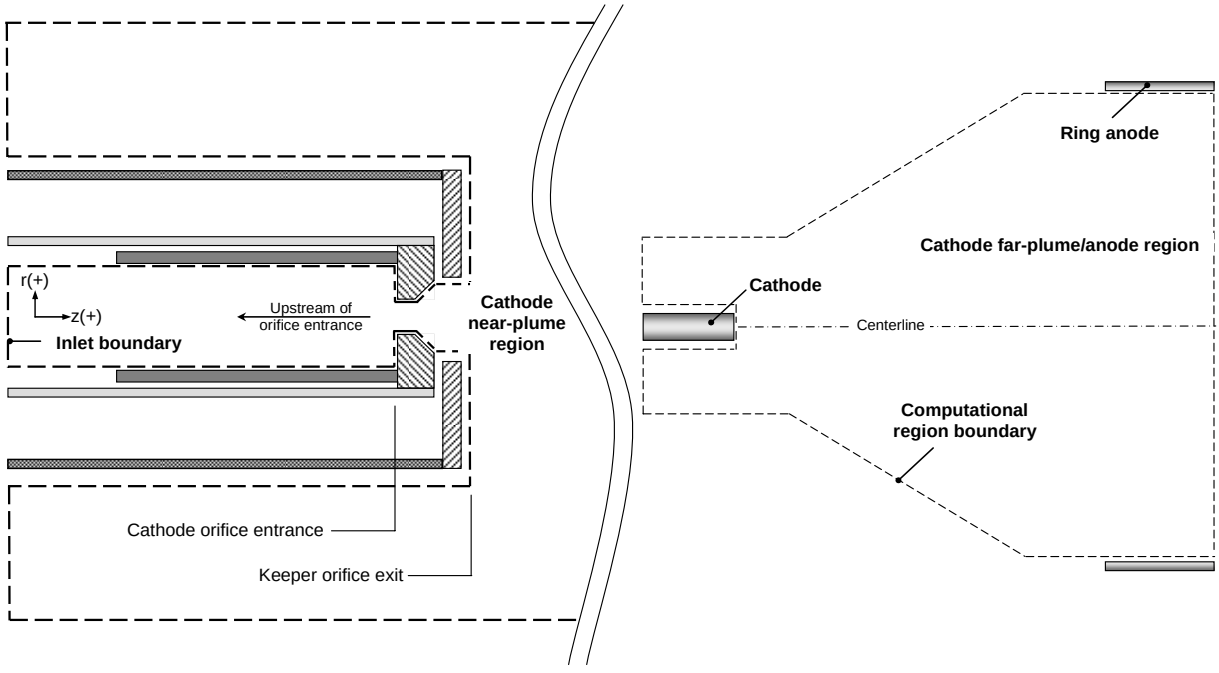

Fig. 1. Schematic of a hollow cathode simulation geometry outlining (by the dashed line) the computational region. Left: Cathode interior and near-plume regions. The "near-plume" is defined as the region of plasma within a radius of a few centimeters downstream of the keeper orifice exit. Right: Far-plume/anode region.

2. Boundary conditions

Ions are assumed to enter the sheath near walls inside the cathode in accordance to the Bohm condition. Bohm ion flux is specified at all other boundaries external to the cathode including the far-plume (outflow) boundaries and the anode. The current density of the absorbed electrons at the sheath along boundaries at voltage V is specified by,

$$\mathbf{j}_{e,abs} \cdot \hat{\mathbf{n}} = -j_{e,th}\, \mathrm{e}^{-e(\phi_p - V)/k_B T_e} \tag{1}$$

where ϕ_p-V is the voltage drop across the sheath. The plasma potential at the grid cell center located adjacent to the wall boundary is denoted by ϕ_p and k_B is Boltzmann's constant. The emitted electron current density from the insert is modeled after the Richardson-Dushman equation for thermionic emission,[10] and includes the effect of the Schottky potential φ_{Sc}, where $\varphi_{eff} \equiv \varphi_{Wf} - \varphi_{Sc}$:

$$\mathbf{j}_{e,em} \cdot \hat{\mathbf{n}} = \tilde{\alpha} T_{em}{}^2 e^{-(e\phi_{eff}/k_B T_{em})}, \qquad \tilde{\alpha} = \alpha f \tag{2}$$

where α=1.2×10^6 A/m^2/K^2. The work function is denoted by φ_{Wf}. The temperature boundary condition T_{em} is prescribed based on available measurements. By contrast to the original numerical simulations of a 1.5-cm, 25-A cathode, results from the 0.635-cm showed that emission enhancement due to the high plasma density conditions is probable. The mechanism was characterized as "sheath funneling." The hypothesis is that when the plasma density is high enough so that the Debye length becomes smaller than the mean pore radius r_p of the emitter the sheath can be funneled into the pores thereby enhancing the effective emission area. In light of the uncertainties associated with the microstructure of the pores (e.g. see Fig 2) the increase in emission area was modeled only simply, by assuming that the plasma served as a singular ion source for the each pore. It was assumed that pores are perfect cylinders with radius r_p and that the sheath penetrates the cylinder a distance h from the pore entrance. The penetration height h was approximated by assuming that the (collisionless) ions enter the pore along straight-line trajectories with a velocity component normal to the emitter surface that equals the Bohm speed $(k_B T_e/m)^{½}$ and a parallel component that equals the ion thermal speed $(k_B T/m)^{½}$, where m is the heavy species atomic mass and T is the heavy-species temperature. This gave an approximate emission enhancement factor f

$$f = 1 + 2b\sqrt{\frac{T_e}{T}}(\zeta - 1), \;\; \zeta > 1 \tag{3}$$

where b=A_p/A_{em} is the ratio of open area (i.e. the sum of all pore entrance areas) A_p over the total emitter surface area A_{em}, and ζ=r_p/λ_D.

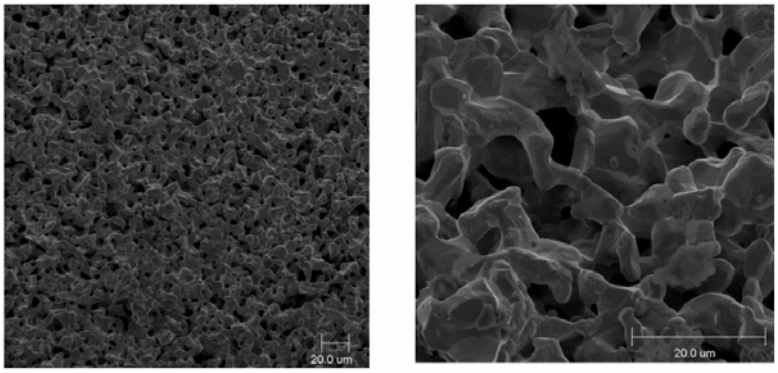

Fig 2. Section of a typical hollow cathode emitter as viewed in different scale sizes.

III. Application of the 2-D Model to Hollow Cathodes for High-Power (>3 kW) Hall Propulsion

A main distinction between hollow cathodes used in Hall thrusters like the BPT-4000 cathode (see Fig. 3) and those used as discharge cathodes at similar power levels in ring-cusp ion thrusters is that Hall thruster cathodes usually operate at higher flow rates. A comparison of typical thrusters and operating conditions is shown in Table 1 below. Since the NSTAR discharge cathode geometry is representative of cathode geometries used in existing Hall

thrusters we present in this section results from simulations of the NSTAR cathode geometry operating at the BPT-4000 3-kW power level (see Table 1). No magnetic field has been applied in the simulations since it has little effect on the plasma inside the emitter region. Moreover, the near-plume region of most Hall thruster cathodes has a significantly lower applied magnetic field compared to ion thruster discharge cathodes.

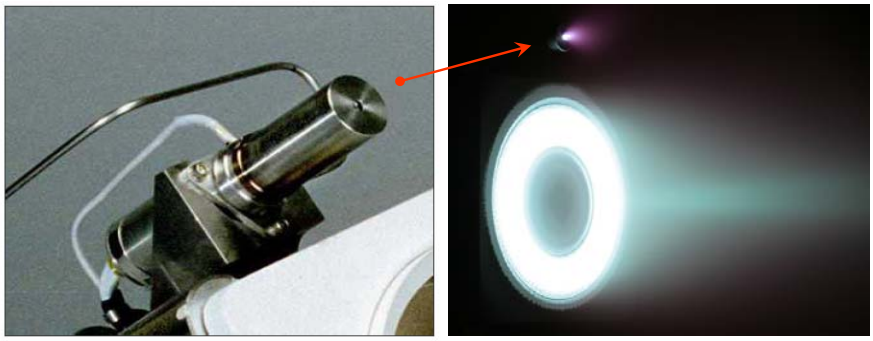

Fig. 3. Aerojet's BPT-4000. Left: The cathode assembly. Right: Operation at 1 kW.

Table 1. Typical operational characteristics of ion engine discharge hollow cathodes compared to a Hall thruster cathode. The 30-cm ion thruster used a discharge cathode with a 0.635-cm diameter cathode tube and the 60-cm thruster used a larger tube, 1.5 cm in diameter.

	Hall Thruster (BPT-4000)		30-cm Ion Thruster	60-cm Ion Thruster
Discharge power (kW)	3.0	4.5	2.3	25.0
Discharge (cathode) current, A	10.0	15.0	13.3	25.0
Cathode mass flow rate, sccm	11.1	15.5	3.7	5.5

B. Internal measurements at different flow rates

Previous internal plasma measurements obtained in the 0.635-cm and 1.5-cm cathodes point to a clear trend: the maximum plasma density and the slope of the density drop-off from the peak value at the axis of symmetry increase with increasing flow rate. Representative measurements at two flow rates for a fixed discharge current are shown in Fig. 4-right inside the 1.5-cm cathode. As shown in Fig. 4-left, similar trends have been observed for the 0.635-cm cathode albeit at lower flow rates. Measurements of the plasma density inside the 0.635-cm cathode operating at >10 sccm have not yet been performed but are part of future experimental work at JPL.

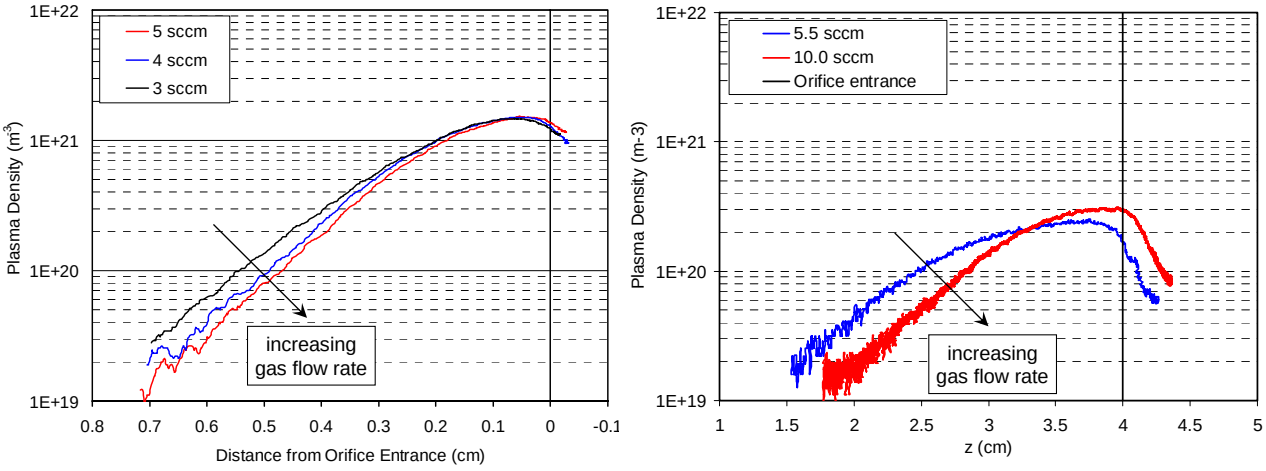

Fig. 4. Axis-of-symmetry measurements of the plasma density inside two discharge hollow cathodes. Left: 0.635-cm cathode operating at 12 A. Right: 1.5-cm cathode operating at 25 A.

C. Numerical simulations

1. *Grid sensitivity calculations*

With higher densities expected at the higher flow rates the resolution of the region near the emitter becomes more critical. Thus, we summarize here the results of grid sensitivity calculations that were performed with the intent to ensure that no unphysical dependencies of the numerical solution exist. A previously obtained simulation result for the NSTAR cathode at 3.7 sccm and 15 A was repeated for two additional grid arrangements. In both cases the original grid (Fig. 5, left) was re-distributed quadratically with radius. In the first case Fig. 5 (top, right) the grid cell adjacent to the emitter boundary was reduced in (radial) size by 4 times, in the second case (bottom, right) by 2 times. The results are compared in Fig. 6. We find that the grid has a negligible effect on the solution. The discrepancy is slightly more evident in the low density regions because the aspect ratio on the computational cells (or the grid conformality) becomes too large to retain the same level of accuracy in the solution.

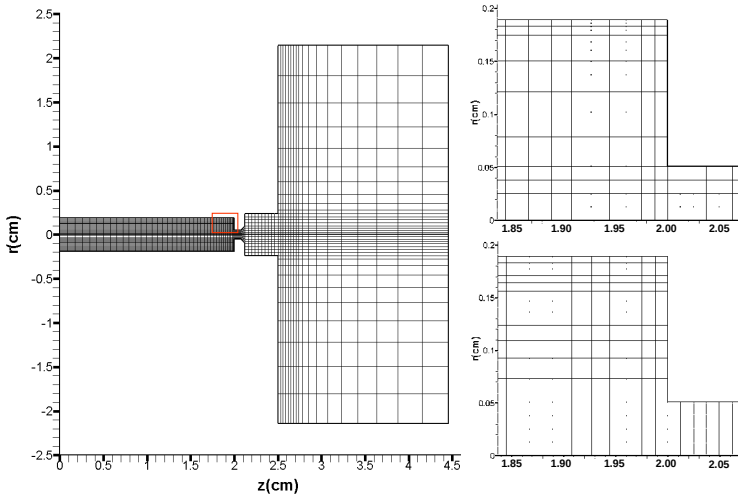

Fig. 5. Left: Global grid arrangement for the hollow cathode grid sensitivity simulations. Right: Close-up views of the near-emitter region showing increased resolution of the computational grid.

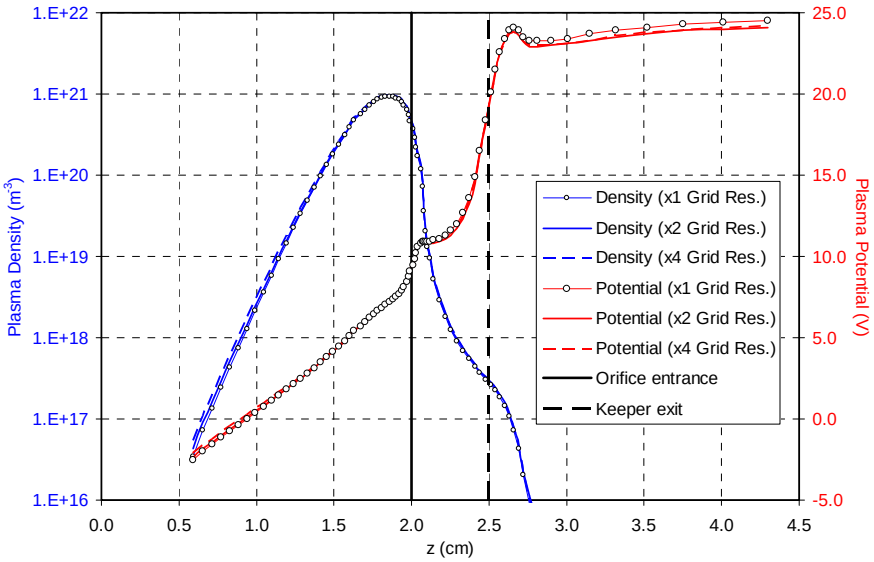

Fig. 6. Axis-of-symmetry results from computational grid sensitivity calculations showing negligible differences in the computed solution when the grid near the emitter is better resolved compared to the original arrangement.

2. Simulations at different flow rates

Numerical simulations of the 1.5-cm cathode performed previously by the authors showed that viscous effects were not negligible in the orifice channel. Upon including the viscous terms the predicted pressure inside the cathode was found to be within 15% of the measured value. By contrast to the viscous solution, the inviscid solution yielded approximately half the measured value. The same assessments of viscous effects are performed in this section for the 0.635-cm cathode. The Reynolds number *Re* is given by,

$$Re \equiv \frac{m\Gamma_n D}{\mu} = \frac{D}{\lambda_{vis}} \tag{4}$$

where the viscosity coefficient μ is given by,[11]

$$\mu = 2.3\times10^{-5}\,\overline{T}^{(0.71+0.29/\overline{T})}\ \ Pa\cdot\sec, \qquad \overline{T} \equiv T/289.7 > 1 \tag{5}$$

with Γ_n denoting the neutral gas particle flux and D is a characteristic cathode dimension. The characteristic viscous length λ_{vis} is shown in Fig. 7 for the 0.635-cm cathode operating point of 5 sccm and 12 A based on the inviscid, steady-state solution. It is seen that *Re* is in the order of unity inside the cathode and orifice. The Knudsen number based on the mean free path for neutral-neutral collisions, λ_{nn}, (Fig. 7, bottom) is found to range between ~1 (inside the orifice) to <0.01 in far upstream regions of the cathode. In general, OrCa2D has been developed to solve the fully-viscous (fluid) momentum conservation law for the neutral gas, as implied in Eq. (6), up to the exit of the cylindrical portion of the orifice. The equation and the numerical approach downstream of the cylindrical section have been discussed elsewhere, and will not be repeated here. In Eq. (6), $\mathbf{\Gamma}_n$ is the neutral gas particle flux vector, n_n and p_n are the neutral particle density and pressure, and $\mathbf{u}_n$, $\mathbf{u}_i$ are the neutral and ion velocities, respectively. The coefficients of viscosity Λ and μ relate normal stresses to $\nabla\cdot\mathbf{u}_n$ and to the rates of extension respectively, and are (usually) related by the simple expression Λ=-2/3μ for Newtonian fluids (barred quantities below denote values per unit mass). Noted is the second term on the right hand side of Eq. (6) which represents the "frictional" force exerted on the neutrals by the ions, with ν_{in} denoting the ion-neutral collision frequency; this term is fundamentally distinct from the viscous terms which represent the transport of momentum in the neutral gas.

$$\begin{aligned}
&\frac{\partial \Gamma_{n,z}}{\partial t} + \nabla\cdot\left(\Gamma_{n,z}\mathbf{u}_n\right) = -m^{-1}\nabla_z p_n + n\nu_{in}\left(u_{i,z}-u_{n,z}\right) + \nabla_z\left(\overline{\Lambda}\nabla\cdot\mathbf{u}_n\right) + \nabla\cdot\left[\overline{\mu}\left(\nabla_z\mathbf{u}_n + \nabla u_{n,z}\right)\right],\ \ \Gamma_{n,z} = n_n u_{n,z} \\
&\frac{\partial \Gamma_{n,r}}{\partial t} + \nabla\cdot\left(\Gamma_{n,r}\mathbf{u}_n\right) = -m^{-1}\nabla_r p_n + n\nu_{in}\left(u_{i,r}-u_{n,r}\right) + \nabla_r\left(\overline{\Lambda}\nabla\cdot\mathbf{u}_n\right) + \nabla\cdot\left[\overline{\mu}\left(\nabla_r\mathbf{u}_n + \nabla u_{n,r}\right)\right],\ \ \Gamma_{n,r} = n_n u_{n,r}
\end{aligned} \tag{6}$$

The "no-slip" condition is implemented at all boundaries on the tangential component of the neutral gas velocity (unless otherwise stated). The normal velocity component is prescribed as

$$\mathbf{u}_n\cdot\hat{\mathbf{n}} = -\frac{\mathbf{\Gamma}_i\cdot\hat{\mathbf{n}}}{\tilde{n}_n} \tag{7}$$

where $\tilde{n}_n$ is the value of the neutral gas density at the center of the cell adjacent to the boundary in question, and $\mathbf{\Gamma}_i$ is the ion flux vector. The condition above assumes that all ions impacting the cathode boundaries neutralize by acquiring a free electron from the surface and return to the plasma as atoms.

A comparison between the viscous and inviscid solutions for the neutral gas flow field exposes the significance of viscosity inside the cathode. The left illustration in Fig. 8 plots velocity vectors obtained as part of the inviscid solution in the vicinity of the high-plasma-density region, and shows clearly that the flow develops circulation in this region. It is shown that much of the centerline flow is turned away from the orifice while all the mass flux to the orifice is provided by the orifice plate ions (returning as neutrals) and those portions of the emitter closest to the orifice plate. In the presence of viscosity the character of the flow field is fundamentally different. No circulation

develops inside the cathode while the velocity flow field upstream of the orifice, where both the gas speed and ionization are sufficiently low, establishes a parabolic profile with radius as expected.

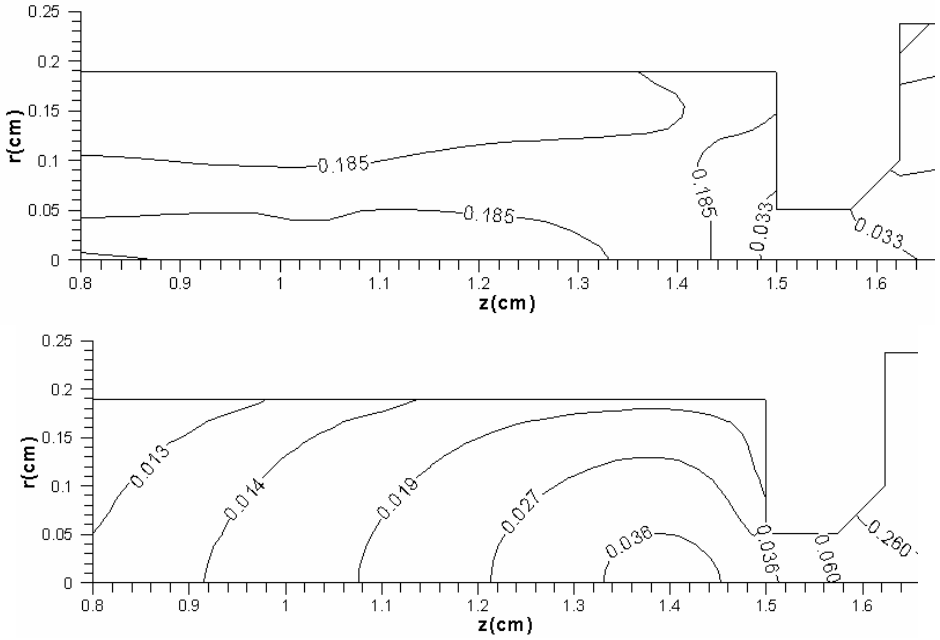

Fig. 7. Contours of characteristic lengths in the 0.635-cm cathode at 5 sccm and 12 A based on the inviscid neutral gas solution. Top: characteristic length for viscosity λ_{vis} (in cm). Bottom: mean free path for n-n collisions λ_{nn} (in cm).

To better elucidate the change in the flow field character between the inviscid and viscous solutions the various forces that act on the neutral flux are plotted in Fig. 9. Specifically, in steady-state, the z-component of the momentum equation (6) above may be re-expressed as follows:

$$\frac{n}{n_n}\nu_{in}\Gamma_{n,z} = -\nabla\cdot\left(\Gamma_{n,z}\mathbf{u}_n\right) - m^{-1}\nabla_z p_n + \nabla_z\left(\overline{\lambda}\nabla\cdot\mathbf{u}_n\right) + \nabla\cdot\left[\overline{\mu}\left(\nabla_z\mathbf{u}_n + \nabla u_{n,z}\right)\right] + \nu_{in}\Gamma_{i,z} \tag{8}$$

I II III IV

Term "I" in Eq. (8) represents the neutral gas inertia, "II" is the pressure gradient, "III" are the viscous terms and "IV" is the ion drag on the neutrals due to charge exchange. The four terms are plotted as a function of axial location along the axis of symmetry in Fig. 9; the left illustration is for the inviscid case and the right is for the viscous case. Most evident is the dominance of the pressure-gradient (normal stresses on the fluid element) and ion-drag forces by comparison to the remaining forces. These two competing forces are largely responsible for the characteristic behavior of the flow field shown in Fig. 8. Also evident is that the pressure-gradient force exceeds the ion drag in the viscous solution, leading to the forward-directed vector field of Fig. 8-right, whereas the opposite occurs in the inviscid solution. The main impact of viscosity therefore has been the rise of the total pressure inside the cathode which allows for a larger pressure-gradient force compared to the inviscid case - sufficiently large to overcome the opposing ion drag and reverse the velocity field in regions of circulation. The rise in the total pressure will be quantified later in this section.

The same evaluation of terms can be made for the ions using the ion momentum conservation law, Eq. (9), where m_e is the electron mass, ν_{ei} is the electron-ion collision frequency, $\mathbf{E}$ is the electric field, p_i is the ion pressure and $\mathbf{j}_e$ is the electron current density.

$$\left(mv_{in} + m_e v_{ei}\right)n\mathbf{u}_i \approx mv_{in}n\mathbf{u}_i = ne\mathbf{E} - \nabla p_i - e^{-1}m_e v_{ei}\mathbf{j}_e + mv_{in}n\mathbf{u}_n \tag{9}$$

Equation (9) may be re-expressed in a form similar to Eq. (8) above as follows:

$$v_{in}\Gamma_{i,z} \approx \underset{\text{I}}{\frac{e}{m}nE_z} - \underset{\text{II}}{\frac{eT}{m}\nabla_z n} - \underset{\text{III}}{\frac{m_e}{m}\frac{v_{ei}}{e}j_{e,z}} + \underset{\text{IV}}{\frac{n}{n_n}v_{in}\Gamma_{n,z}} \tag{10}$$

In Eq. (8) the ion pressure gradient term has been approximated by the plasma density gradient times the ion temperature, T (which is assumed to equal the neutral gas temperature). The various terms in Eq. (10) are compared in Fig. 10 for the inviscid and viscous cases. We clarify here that by "viscous case" we refer to the addition of neutral gas viscosity only; by comparison, ion viscosity is assumed negligible. Both cases show the dominance of the electric field, electron drag and neutral drag terms on the development of the ion flow inside the cathode, with the ion pressure playing a lesser role.

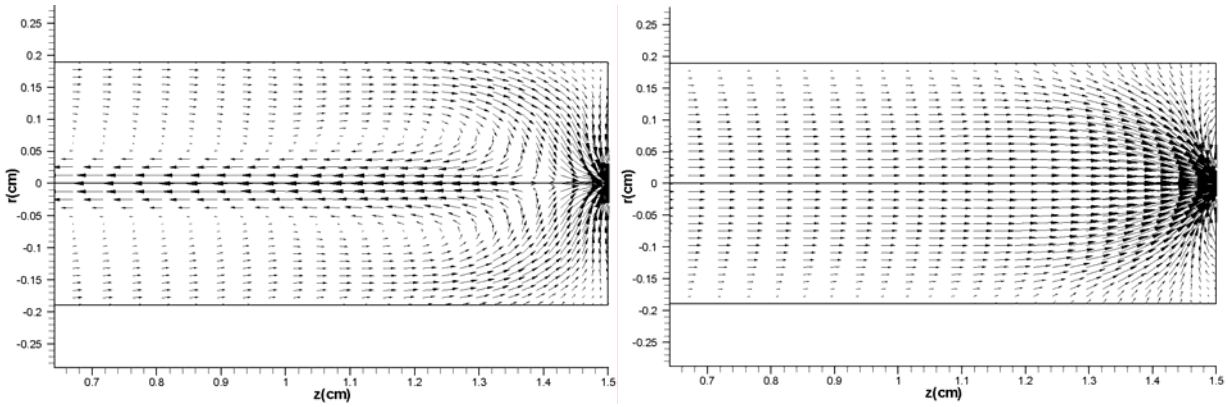

Fig. 8. Neutral gas velocity vector field (Note: the orifice entrance is at z=1.5 cm). Left: Inviscid solution. Right: Viscous solution with no-slip boundary conditions everywhere in the fluid domain.

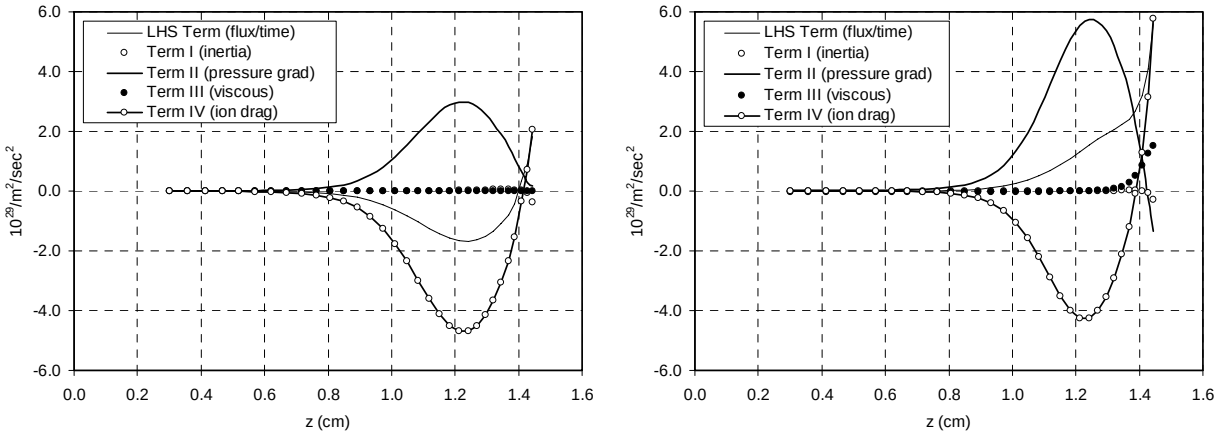

Fig. 9. Comparison of terms in the neutral gas momentum equation. Left: Inviscid solution. Right: Viscous solution with no-slip boundary conditions everywhere in the fluid domain.

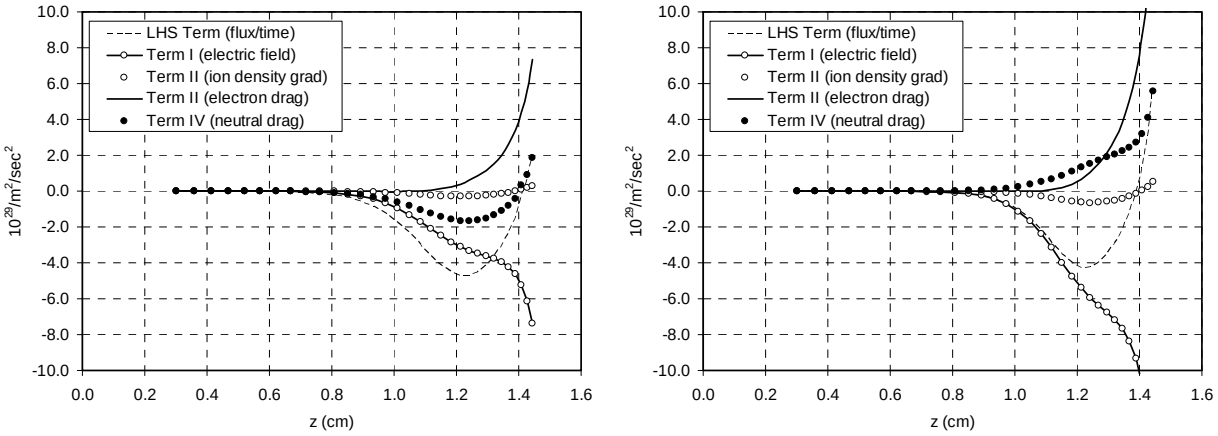

Fig. 10. Comparison of terms in the (inertia-less) ion momentum equation. Left: Inviscid solution. Right: Viscous solution with no-slip boundary conditions everywhere in the fluid domain.

As proposed previously the main effect of viscosity has been the rise of the total pressure inside the cathode. This is quantified in Fig. 11 below which plots the computed pressure 1.3 cm upstream of the orifice entrance for three flow rates. Also plotted are measured values at a location of about 13 cm upstream of the orifice where the propellant is injected. Approximately the first 5 cm (of the total 13 cm) upstream of the orifice comprise the emitter and cathode tube regions while the remaining ~8 cm consist of a tube almost 2 cm in diameter. It is therefore possible that additional rise in the pressure may occur beyond the 1.5-cm computational region presently allowed in the numerical simulation. The discrepancy between the measured and computed values is found to be approximately 30%. Also shown are results for the fully inviscid case which clearly underestimates the measured value at 5 sccm by more than 60%. Much discussion in the literature has revolved around the proper boundary condition in low Reynolds number flows with Knudsen number in the order of unity. We therefore also present results from two additional simulation cases that incorporate the viscous terms, as in the original fully-viscous case with "no-slip" boundary conditions at the walls, but employ a "free-slip' boundary condition along the cathode orifice walls (instead of "no-slip"). The simulations were performed to assess, in part, the impact of the boundary condition choice in regions where the gas flow is transitional. This solution yields a lower pressure than both the measured and fully-viscous cases but higher than the inviscid case. The comparisons suggest that the fully-viscous approach provides cathode pressure values that are the closest to the measured values.

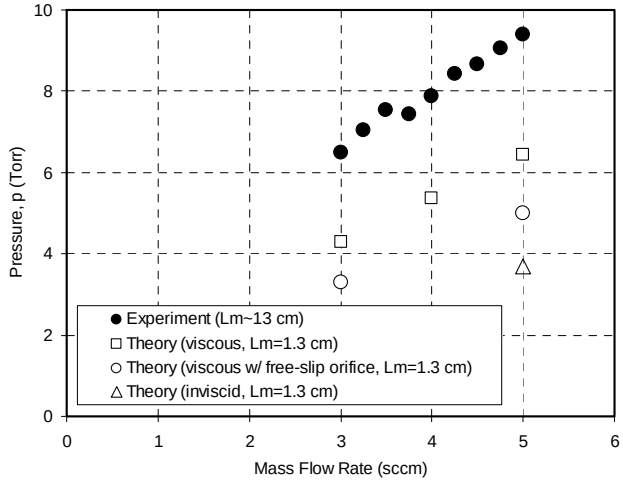

Fig. 11. Comparison between measured and computed values of the cathode pressure. ("Lm" denotes the distance upstream of the orifice entrance where the value(s) are shown.)

Finally, results for the plasma density from the fully-viscous simulations are compared with the measurements of Fig. 4-left (at 3, 4 and 5 sccm and 12 A of discharge current) in Fig. 12 along the axis of symmetry. Also shown is the computed result for the Hall thruster cathode typical operating condition of 11.1 sccm and 10 A. Both the quantitative and qualitative comparisons with the measurements are favorable. Some of the more subtle discrepancies between theory and experiment depicted in Fig. 12 will be the subject of near-term studies.

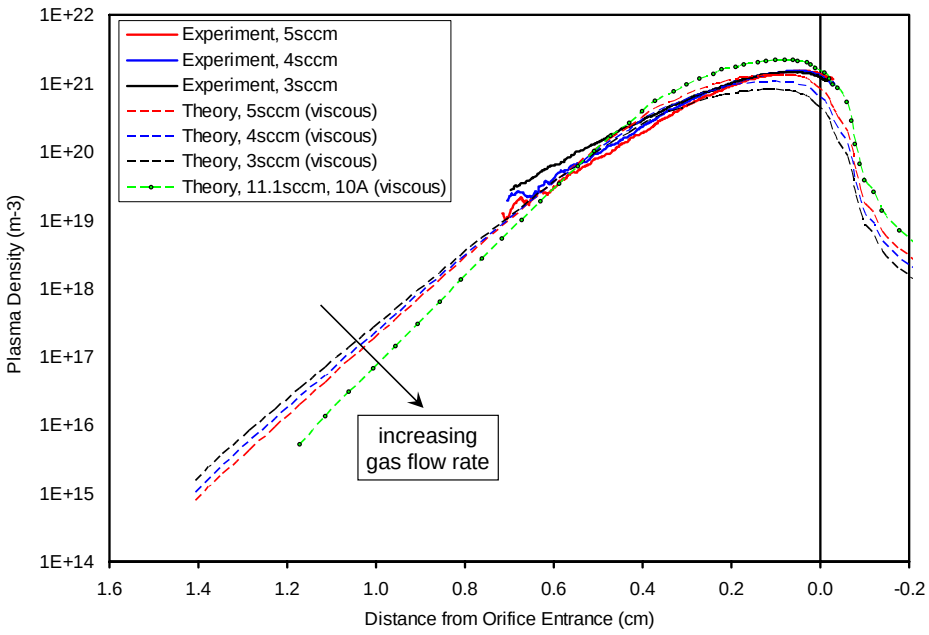

Fig. 12. Measured and computed profiles of the plasma density along the axis of symmetry at various operating conditions.

IV. Conclusions

The 2-D model of the partially-ionized inside hollow cathodes OrCa2D has been applied to model the plasma inside a cathode operating at various flow rates including one operating point typical of a 4.5-kW Hall thruster cathode. Hall thruster cathodes normally operate at more than twice the gas flow rate compared to discharge hollow cathodes used in ion propulsion, at comparable power levels. It is found that for all flow rates examined neutral gas viscosity is an important mechanism in these devices that can not be neglected, in close agreement with previous findings from numerical simulations of a larger (1.5-cm) discharge hollow cathode. This is largely due to the fact that the neutral gas temperature can exceed 2000 K in many regions of the cathode where the gas flow velocity is relatively small and the viscosity is high. The computed cathode pressure follows the same trend with flow rate as the measurement taken approximately 13 cm upstream of the entrance to the cathode orifice. Measurements of the plasma density inside cathodes at varying geometries and gas flow rates point to a common trend: the maximum plasma density and the slope of the density drop-off from the peak value increase at the axis of symmetry with increasing flow rate. The numerical simulations reproduce the observed trend and provide a quantitative account of all the forces responsible for such trends in the plasma. The simulation results also provide quantitative insight on the characteristic features of the neutral gas velocity flow field in these devices.

Acknowledgments

The research described in this paper was carried out by the Jet Propulsion Laboratory, California Institute of Technology, under a contract with the National Aeronautics and Space Administration in support of the In-Space Propulsion Technology Program.

References

[1] Bober, A. S., and Maslennikov, M., "SPT in Russia-New Achievements," Proceedings of the 24th International Electric Propulsion Conference, pp. 54-60, (1995).

[2] Naval Research Laboratory, Press Release, Oct. 29, 1998.

[3] Hofer, R. R., Randolph, T. M., Oh, D. Y., Snyder, J. S., and de Grys, K. H., "Evaluation of a 4.5 kW Commercial Hall Thruster System for NASA Science Missions," AIAA Paper 06-4469, July 2006.

[4] Polk, J. E., Anderson, J. R., Brophy, J. R., Rawlin, V. K., Patterson, M. J., Sovey, J., and Hamley, J., "An Overview of the Results from an 8200 Hour Wear Test of the NSTAR Ion Thruster," AIAA Paper 99-2446, June 1999.

[5] Sengupta, A., Brophy, J. R., and Goodfellow, K. D., "Status of the Extended Life Test of the Deep Space 1 Flight Spare Ion Engine after 30,352 Hours of Operation," AIAA Paper 03-4558, July 2003.

[6] Polk, J. E., Marrese, C., Thornber, B., Dang, L., and Johnson, L., "Temperature Distributions in Hollow Cathode Emitters," AIAA Paper 04-4116, July 2004

[7] De Grys, K., Welander, B., Dimicco, J., Wenzel, S., Kay, B., Kayms, V., and Paisley, J., "4.5 kW Hall Thruster System Qualification Status," AIAA Paper 05-3682, July 2005

[8] Mikellides, I. G., Katz, I., Goebel, D. M., and Polk, J. E., "Hollow Cathode Theory and Experiment. II. A Two-Dimensional Theoretical Model of the Emitter Region," *J. Appl. Phys* [online], Vol. 98, 2005, p. 113303.

[9] Mikellides, I. G., Katz, I., Goebel, D. M., and Polk, J. E., "Theoretical Model of a Hollow Cathode Plasma for the Assessment of Insert and Keeper Lifetimes," AIAA Paper 05-4234, July 2005.

[10] Dushman, S., "Electron Emission from Metals as a Function of Temperature," *Phys. Rev*., Vol. 21, No. 623, 1923.

[11] Reid, R. C., Prausnitz, J. M., and Sherwood, T. K., *The Properties of Gases and Liquids*, 3rd ed., McGraw-Hill, New York, 1977, pp. 402-403.